Aerodynamic studies over a manoeuvring UCAV 1303 configuration

M. S. Chandrasekhara
mchandra@nps.edu
B. K. McLain
Department of Mechanical and Aerospace Engineering
US Naval Postgraduate School
Monterey, USA

ABSTRACT

The flow past an unmanned combat air vehicle (UCAV) 1303 was investigated in a water tunnel in an effort to understand the complex flow field. The UCAV 1303 is characterised by a non slender, 47° swept-leading-edge delta wing, with a cranked trailing edge, a cropped wing tip and a fuselage. It also has no vertical tail. Dye visualisation pictures and five-axis strain gage load data were obtained on a 1:72 scale model in both steady flow and while the model executed pre-programmed manoeuvres. From the strain gage data, body axis force and moment data were derived. In addition to some similarities, comparison of the flow features observed with those of more well known slender delta wing flows showed some remarkable differences such as tip-stall, the presence of two like-sense vortices on the same side of the wing, their simultaneous spiral and bubble bursting. This paper predominantly discusses the flow visualisation results and attempts to correlate the load data to some of the observed flow features.

Paper No. 3662. Manuscript received 12 November 2010, accepted 14 June 2012.

https://doi.org/10.1017/S0001924000008095 Published online by Cambridge University Press

NOMENCLATURE

C_m	pitching moment coefficient
C_n	normal force coefficient
C_{RM}	rolling moment coefficient
C_S	side force coefficient
C_{YM}	yawing moment coefficient
c	chord
$\bar{c}$	mean aerodynamic chord
N	normal force
PM	pitching moment
Re	Reynolds number based on mean aerodynamic chord
RM	rolling moment
S	side force
U_∞	freestream velocity
x/c	distance along the body
YM	yawing moment
α	angle-of-attack
$\propto$	dimensional pitch rate
α^+	non-dimensional pitch rate
$\Delta\alpha$	increment in angle-of-attack $\frac{\dot{\alpha}c}{U_\infty}$
ϕ	roll angle
ρ	density

1.0 INTRODUCTION

This study pertains to the popular Unmanned Combat Air Vehicle (UCAV) 1303 geometry. UCAVs have already proven effective in recent times. Their pilotless operation also means that the advantages of aerodynamic phenomena such as dynamic lift can be implemented and effectively exploited for their super-manoeuvreability and other capabilities. However, the absence of a vertical tail, control surfaces and a stealthy design makes such UCAVs look like a flying wing and has meant that they operate on the fringes of the stability boundary. In fact, a study[1] of the aerodynamics of the UCAV 1301 ((the predecessor to UCAV 1303) has shown that it is unstable. A UCAV can be expected to perform unusual manoeuvres depending on the mission being performed. Even in normal flight, manoeuvres may become necessary during gusts and in evading incoming threats. Clearly, stability and the required control authority are major issues that should be addressed during design, lest an unstable and uncontrollable aircraft may be lost and even end up in the wrong hands. Hence, it is important to establish the unsteady aerodynamic behaviour of a manoeuvring UCAV 1303. Towards this goal, a UCAV 1303 model was tested in the Naval postgraduate School (NPS) water tunnel using dye injection for flow visualisation and a five-component strain gage balance for load data.

The aerodynamic and flow characteristics of conventional delta wings with large sweep angles (above 50°) are well known. The UCAV 1303 uses a non slender delta wing design and has been studied recently by a group of researchers in the TTCP program. Reported research[2,3,4] has documented some flow physics information and established the basic differences in steady flow between non slender delta wings and the well studied slender delta wings. A UCAV 1303 model design uses 47° leading-edge sweep and a 30° cranked trailing

https://doi.org/10.1017/S0001924000008095 Published online by Cambridge University Press

edge. This configuration is popular, but literature reveals conflicting physical flow aspects in its aerodynamics. Furthermore, the fluid dynamics of a non slender delta wing design seems to be heavily influenced by whether a fuselage is present or not. Some load data is also available in steady flow, but the aerodynamics information becomes very limited when the fuselage is included or unsteady motion is involved. For the model with the fuselage OI[5] observed just one instance of a leading edge vortex. He also observed a startling result that when the model surface was painted for PIV use and repainted for flow visualisation studies subsequently, the vortical structure actually disappeared. This suggests that surface geometry may also play a major role in testing at lower Reynolds numbers, perhaps due to the incidental leading edge radius effects. Others[4,6], however, have typically reported two vortices over a non slender delta wing. There is general consensus[2] that a non slender wing flow is only moderately sensitive to Reynolds number, unless the leading edge is rounded. Still, the strong spanwise flow on the low sweep wing makes the flow interactions very complex. For delta wings of low leading edge sweep angles, Gursul, *et al*[2] have provided comprehensive flow details and discussed the differences in leading edge vortex behaviour compared to that over slender delta wing flows. Primarily, the vortex is not as dominant, the spanwise flow affects the formation and behaviour of the vortex; and its breakdown is far less clearly discernible. The flow still rolls up over the wing and as a result, the vortex forms at a very low angle-of-attack, but it bursts diffusely at lower angles unlike slender delta wing vortices. Gursul, *et al*[2] and Yaniktepe and Rockwell[3] have provided some details of the vortex breakdown mechanism (including its unsteady nature arising from shear layer instabilities), the evolution of secondary structures from shear layer separation and reattachment over the wing surface and discussed elements of the surface flow topology.

The flow details that have now emerged are the following: Unlike slender delta wing flows which are dominated by large, conical leading-edge vortices that are primarily responsible for the enhanced lift observed, the vortices in the non slender wing case are not so well defined and not as strong. When present, they also contribute to some lift (and its rapid loss) depending on the angles of attack of their formation and breakdown. The slender delta wing flow vortices form at angles of attack around 10° and higher as the vortical boundary-layer rolls up from the wing underside and separates along the leading edge. The non slender delta wing vortical structures can develop at very low angles-of-attack and some times, a dual vortex structure also forms[4,6]. Often times, these structures are found to be elongated[2,3]. The origin of the dual vortices has been traced to secondary separation[2] and there is agreement that the second structure is weaker. From the description in the literature, this second vortex appears to be more like the tertiary structure and hence, the dual vortices have the same sign. The vortices remain close to the surface of the non slender delta wing even at moderate angles of attack leading to a strong viscous/inviscid interaction. In addition, the vortex trajectory is known to sway away from or towards the wing centre-plane with increase in angle-of-attack. The vortices also breakdown at lower angles of attack compared to those on a slender delta wing.

The aerodynamic loading on a UCAV 1303 has been studied somewhat more extensively[7,8,9] both computationally and experimentally at higher speeds in wind tunnels than in the above (water-tunnel investigations) in an effort to validate CFD codes for various turbulence models, but only under steady flow conditions. A notable finding is the appearance of pitch-breaks in the pitching moment distributions, which are attributed to tip-stall. OI[5] attempted to establish validity of using a water tunnel for such high Reynolds number flows and also found some evidence of tip-stall at a very low angle-of-attack, $\alpha = 2{\cdot}5°$. He concluded that

https://doi.org/10.1017/S0001924000008095 Published online by Cambridge University Press

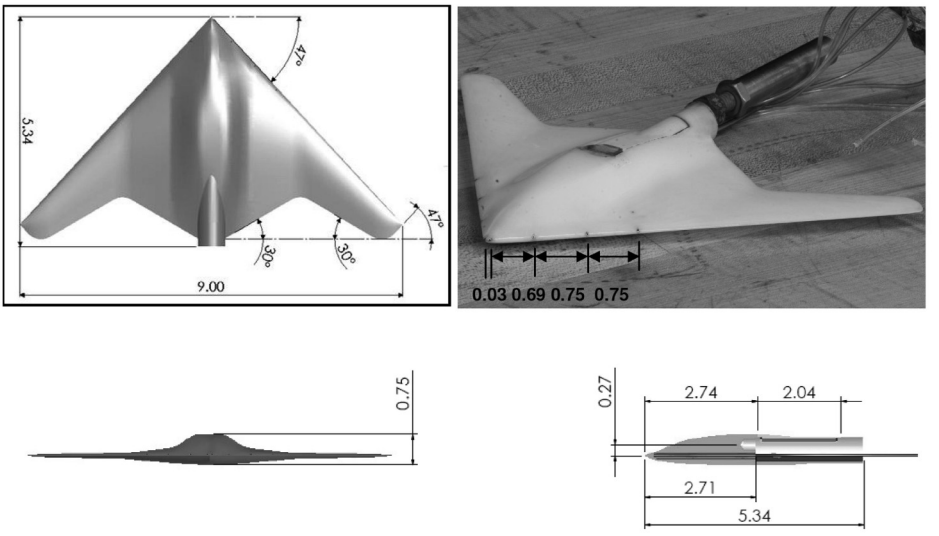


Figure 1. UCAV 1303 model with dimensions (inches), and dye-ports (distances along the leading edge) as used in the NPS water tunnel.

the sharp taper of the UCAV 1303 wing results in a low tip chord based Reynolds number and hence conjectured that tip-stall may always be present. He also observed that the wing stalled first at the tip and the stall later moved inboard as angle-of-attack is increased. But, as stated earlier he did not find a strong evidence for the existence of a primary vortex in the flow. In almost direct contrast to this, in their studies of the unsteady aerodynamic loads on the vehicle, Cummings *et al*[1] have verified an observation by Cunningham[10] that over a pitching UCAV 1301 model that occurrence of pitch-break is a major feature and attribute it to the vortex behaviour. For a manoeuvring UCAV, such events can give rise to unacceptable lift and pitching moment breaks which can lead to potentially hazardous instabilities. Despite the above, a manoeuvring UCAV also experiences dynamic lift, which is clearly desirable, however, its adverse pitching moment fluctuations are not.

Unsteady manoeuvres can lead to the occurrence of the dynamic stall phenomenon on the wing. The benefits of dynamic stall and the extra lift associated with it are important at all flight speeds and are well documented[13]. Dynamic lift during a manoeuvre can be especially valuable while evading a perceived threat. With the human out of the cockpit and the effective elimination of the g-load restrictions during a manoeuvre, the UCAV can be designed to exploit dynamic stall to become a super manoeuvreable platform. If the flow can be suitably controlled and the undesirable effects of dynamic stall mitigated by passive means, flying under such conditions can become a viable option for the UCAV flight envelope.

Towards this ultimate objective, McLain[11] and Chua[12] both tested a blended wing-body UCAV 1303 model in the NPS water tunnel initially under both steady and unsteady flow conditions. The model was taken through selected unsteady motion histories. So, one could expect to see some of the above described flow characteristics and additional ones due to presence of the fuselage. The results to be presented here draw from these works. The overall study is concerned with establishing the manoeuvre-aerodynamics characteristics of the UCAV about which little is known presently. This paper details some of the commonalities and differences observed when compared to the plain non slender wing flow.

https://doi.org/10.1017/S0001924000008095 Published online by Cambridge University Press

2.0 DESCRIPTION EXPERIMENT AND TECHNIQUES

2.1 Model description

The US Air Force (AFRL) provided the CAD geometry file for the UCAV 1303 tested. Figure 1 shows a dimensional sketch of the model at a scale of 1:72. The fuselage was also included in the original geometry file, which differentiates the present studies from that of flow over plain non slender delta wings. The engine and flow through it were not simulated. Two models were built for this investigation; one for flow visualisation and the other for load data using a five-component strain gage balance. The models were exact replicas of the UCAV 1303 design fabricated using rapid prototyping techniques and had smooth, very fine polyurethane coat finish. Thus, the actual model dimensions correspond to this scale ratio, with only the limitations of the manufacturing process affecting the final values when very small dimensions are concerned. (The leading edge radius distribution was measured to be 1/64in. for most part due to the small scale, although the original configuration has a variation that is expected to be as shown in Fig. 2 of Wong, *et al*[9] who also made the model from the same geometry file.) Both NPS models were identical; the wing span was 9in, root chord 5·34in (with a nominally mean aerodynamic chord c of 3·54in) and the fuselage 0·75in thick respectively. The leading-edge sweep was 47°, the trailing edge was cranked with sweeps of ±30° and ±47° as seen. The models were tested in the NPS water tunnel (Rolling Hills Research Corp. Model 1520) whose dimensions are 15in × 20in × 60in. Thus, blockage was not significant at all angles of attack.

The flow visualisation model contained eight symmetrically located dye ports, 0·024in (0·6mm) in size, placed symmetrically on either side of the central plane at distances of 0·5%, 11%, 22% and 33% of leading-edge span (≈ 6·5in) starting from the apex of the model. This allows documenting the blended wing body junction flow. The dye tubes were routed inside the model through specially milled channels which were then properly sealed to be flush with the lower surface. Additionally, a movable dye tube was used as needed to identify the flow features at specific locations ranging from underneath the starboard side wing leading edge to behind the trailing edge outside of the model.

The load study model was fabricated in two pieces and housed a water-proofed internal strain gage balance to measure normal force (N), side force (S), pitching moment (PM), rolling moment (RM) and yawing moment (YM). The second piece which covered the balance was a portion of the original fuselage to maintain a smooth body exterior. The two-piece design facilitated attachment/removal of the internal balance at the mean aerodynamic chord location and ensured proper fit. The balance was attached firmly with screws to an integral frame inside the model.

2.2 Description of the experiment

As stated earlier, the experiments were conducted in the NPS 15in × 20in water tunnel. It is a free surface, open channel flow facility and hence the model is held upside down in order to eliminate any free surface effects during pitch-up manoeuvres. Thus, pitch-up here requires that the model nose tip be moved down. The model is held by a C-strut with a three-axis motion controller system, driven by stepper motors and gears, permitting any desired movement. Special care was taken during design of the model mounting and support mechanism to eliminate differential motion between the C-strut and the model and to insure one-one correspondence of the model motion with that of the strut. Both the water tunnel and C-strut are controlled by vendor supplied software.

https://doi.org/10.1017/S0001924000008095 Published online by Cambridge University Press

The flow visualisation studies were conducted using food coloring as dye. Five different food colour concentrates (red, green, yellow, blue and black) were diluted with water to be neutrally buoyant dye mixtures and stored in five (of six) pressurised canisters that are a part of the tunnel. An individual valve regulated the pressure in each canister and was carefully adjusted to maintain near zero momentum at each dye-port outlet on the model at all angles of attack. In this experiment, the same coloured dye was supplied to corresponding outlets on the starboard and port sides of the model by using a splitter. Most times, the black dye was used externally as needed by setting up the injection tube as a movable wand to explore flow details, such as wing-tip stall, or to verify if the underside flow rolled up when a vortex was produced, etc. Two, Nikon (standard) digital D80 cameras equipped with zoom lenses were set up on tripods for recording the flow; one on the starboard side flow views and the other at the bottom of the tunnel for plan views of the flow (recall that the model is inverted). Flood lights were used for illumination. The camera shutters were remotely triggered simultaneously, for unsteady flow experiments custom developed LabVIEW based software and integrated hardware were also used. The camera trigger control system consisted of modified Nikon D80 remote external shutter control MC-DC1 with a cable attached to the camera internal contacts. Software was developed in-house for unsteady flow visualisation experiments which used the phase locking technique. The software read the encoder and output a signal from an attached (National Instruments NI 6210) interface card when a match occurred with a pre-selected value with no measurable delay at the rates tested. More details of the arrangement can be found in Ref. 12. A large number of flow images, at different angles of attack in steady flow and unsteady flow were recorded. The unsteady flow experiments were conducted with a non-dimensional pitch rate defined as $\propto^{+} = (\dot{\propto}\bar{c})/U_{\infty}$, where $\dot{\propto}$ is the pitch rate in radians/sec, $\bar{c}$ is the mean aerodynamic chord and U_{∞} is the tunnel freestream velocity. (Other rates- non-dimensional roll and yaw rates are defined likewise.) A movie of the dye-flow was obtained at a very slow pitch rate (≈ 0·001 corresponding to a physical pitch-up of 0·05deg/sec for U_{∞} = 6in/sec) while pitching from 0 – 30 or 0 – 35° to see the flow evolution with angle-of-attack. At such slow rates, it seems reasonable to expect that steady state conditions prevail and this method enables a faster way of acquiring steady flow data without introducing spurious flow features.

A five-component (RHRC) internal strain gage balance instrumented model was used for load measurements[14]. The internal balance consisted of a single rolling moment section (RM), two pitching moment sections (PM1 and PM2) and two yawing moment sections (YM1 and YM2)[14]. The diameters of all sections were 0·5in. Each section used four semiconductor strain gages connected using a full Wheatstone bridge. The balance was waterproofed using a combination of thin plastic coating and RTV (silicone rubber) to allow adequate functionality in a water submerged environment[14]. The 1,000Ω semiconductor strain gages had a gage factor of 145 and provided measurements up to a maximum loading of 15in-lbs in the pitch plane moment, 4in-lbs maximum yaw plane moment and 2·5in-lbs of torque. The internal balance signals generated during testing were conditioned and balanced using an eight-channel Model 2100 Strain Gage Conditioner and Amplifier. The output lines were filtered and sent to a National Instruments PCI-MIO-16XE-10 S/D conversion board that provided guaranteed rates up to 100kilo-samples/sec per channel before processing by the data acquisition/reduction software. The balance was calibrated as per the procedure described in the balance calibration manual[14]. A special fixture was constructed for calibration and weights ranging from 0·002lb to 0·22lb (1gm to 100gm) were used. The RHRC custom software provided the necessary sensitivity coefficients, which were then used to calculate the load and moment coefficients in the actual experiments.

https://doi.org/10.1017/S0001924000008095 Published online by Cambridge University Press

Table 1
Internal strain gage balance sensitivity

Force/Moment	Sensitivity
N	2·4V/lb
S	16·8V/lb
PM	5·0V/in-lb
RM	16·4V/in-lb
YM	10·2V/in-lb

Both steady and unsteady flow load data were obtained. The experiment was controlled by RHRC software that also conducted tare tests for each case and generated a file that was later used by their data processing software for generating the actual loads and moments. In the unsteady manoeuvre studies, the data were ensemble averaged while the model executed specific manoeuvres. Analysis of data acquired over as many as 100 runs led us to conclude that ensemble averages over 20 runs were sufficient to yield stable data. Typical manoeuvres consisted of simple transient pitch-up at different rates and freestream speeds. This paper will restrict the results discussed to steady flow data and dynamic pitch-up manoeuvre results; however some steady flow visualisation data at selected roll angles at angles of attack will also be reviewed.
The experiments were conducted for the following conditions:

Table 2
Experimental conditions

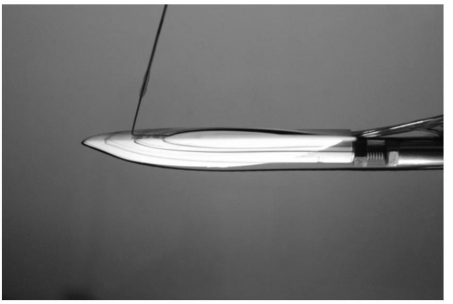
U_∞	2in/sec	6in/sec	10in/sec	14in/sec
$Re_{\bar{c}}$	$4{\cdot}5 \times 10^3$	$1{\cdot}3 \times 10^4$	$2{\cdot}3 \times 10^4$	$3{\cdot}1 \times 10^4$
Pitch Angles, α	0° – 35°	0° – 30°	0° – 30°	0° – 30°
α^+		0·00, 0·05, 0·10, 0·15	0·00, 0·05, 0·10	0·00, 0·05
$\Delta\alpha$		2°	2°	2°
Roll Angles, ϕ		0° – 30°	0° – 30°	0° – 30°

The experimental uncertainties were estimated in the usual manner by including the uncertainties in each major component that forms the quantity measured and are listed in Table 3.

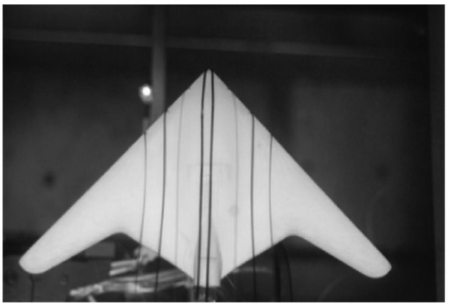
Table 3
Measurement uncertainties

Parameter or coefficient	% Uncertainty
U_∞	±4%
ρ	±0·2%
Normal Force	±2%
Side Force	±0·5%
Moments	±1%
C_n	±5%
C_m	±3%
C_S	±1%
C_{YM}	±3%
C_{RM}	±3%

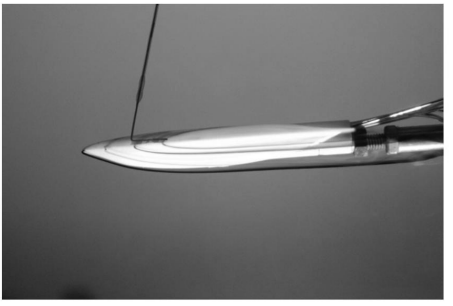
https://doi.org/10.1017/S0001924000008095 Published online by Cambridge University Press



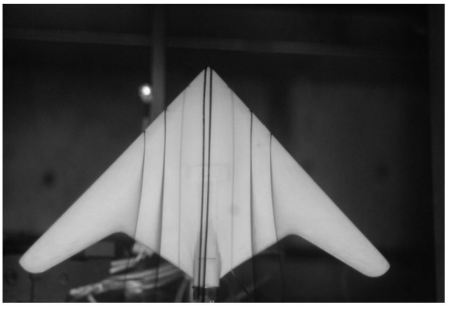
α = 2°



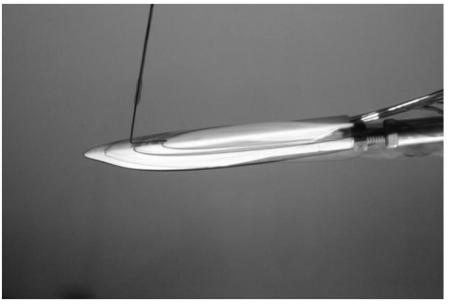
α = 2°



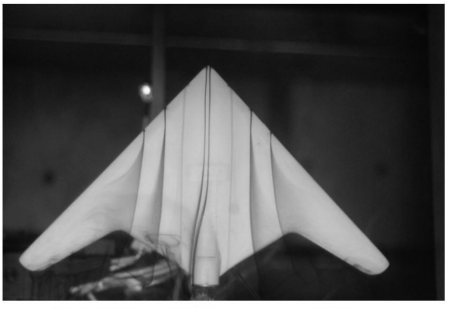
α = 4°



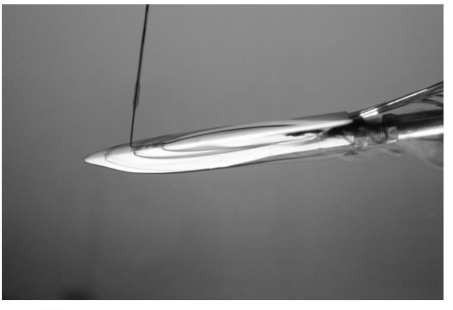
α = 4°



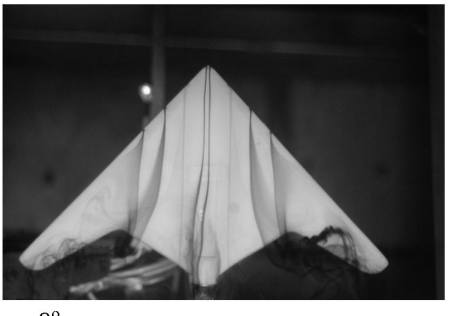
α = 6°



α = 6°

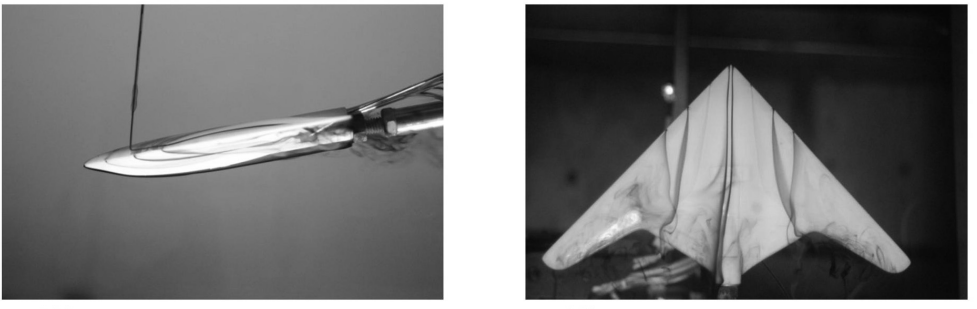


α = 8°



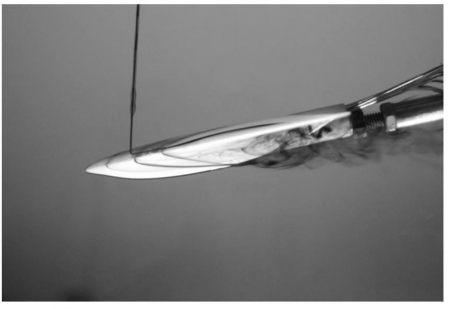
α = 8°

https://doi.org/10.1017/S0001924000008095 Published online by Cambridge University Press

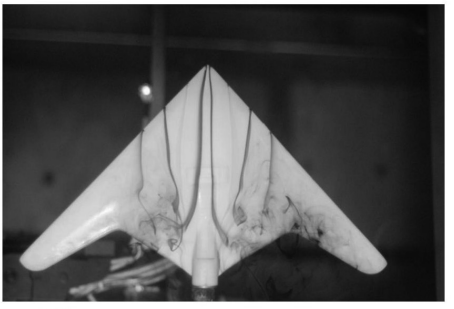


α = 10°

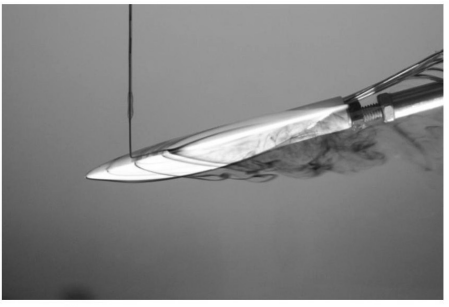
α = 10°



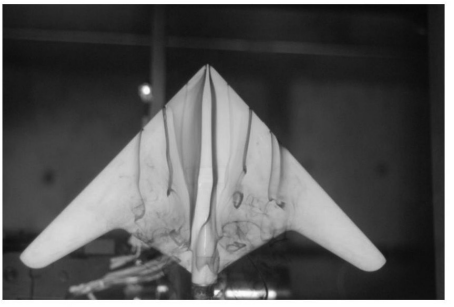
α = 12°



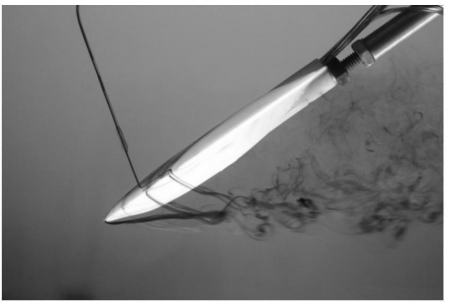
α = 12°



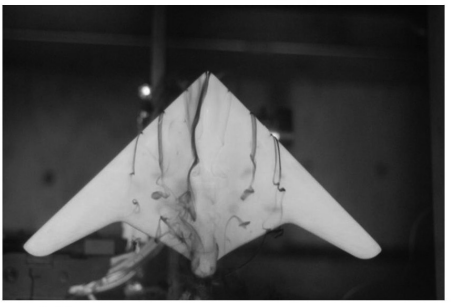
α = 15°



α = 15°



α = 35°



α = 35°

Figure 2. Flow visualisation images at U_∞ = 2in/s, Re = $4{\cdot}1 \times 10^4$.

https://doi.org/10.1017/S0001924000008095 Published online by Cambridge University Press

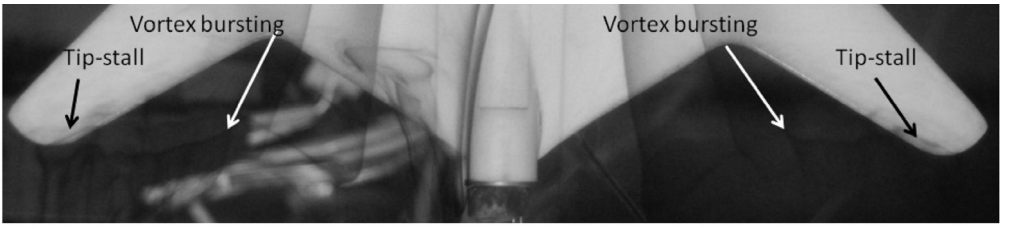
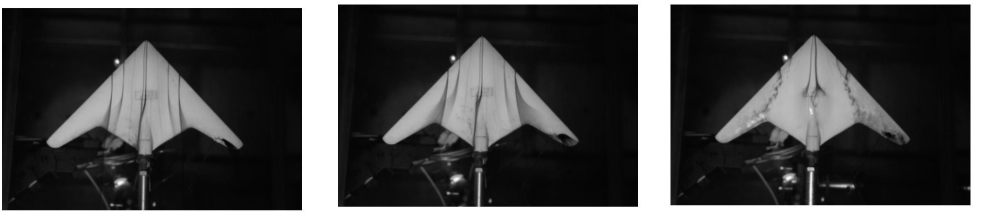


Figure 3. Close-up of tip-stall from trailing-edge crank vortex bursting in wake, Re = $4{\cdot}1 \times 10^4$, $\alpha = 6°$, steady flow.



$\alpha = 4^o$ $\alpha = 6^o$ $\alpha = 10^o$

Figure 4. Tips stall onset flow visualisation, Left: No tip-stall. Middle: Onset, Right: Reverse flow following onset (arrow: dye injection point) Re = $1{\cdot}3 \times 10^4$.

3.0 RESULTS AND DISCUSSION

3.1 Tip-stall

Steady flow images are presented in Fig. 2 for a velocity of 2in/s, Re = 4,100 for angles of attack ranging from 0° to 35°. In these (see side views in the left column), the black dye was introduced (at around the red dye location on the underside) from a bent tube near the wing leading edge to visualise the leading edge vortex roll up. For α up to 4°, these images show (top two rows) near perfect symmetry of the flow over the wing, with the streamlines curving slightly towards the wing tips. A slight spanwise flow is evident for the non-apex ports (e.g. red dye, $\alpha = 2 – 6°$) in the planform flow views. It originates at about the same distance from the leading edge in the dye flow and moves progressively upstream as the angle-of-attack is increased to higher values. Side views of the flow show the dye to be flowing straight into the wake. Since the dye streak diameter (of 0·024in) was larger than the local boundary-layer thickness at each dye-port, both potential and viscous flow regions were incidentally thus visualised, and both spanwise and streamwise flows recorded in these images. The inner portion spreads in the extremely thin three-D spanwise boundary layer (and it appears, following the local skin friction lines) whereas the rest followed the external potential flow. The apex flow (blue dye) leaves the surface past the maximum canopy height (side views, for $\alpha = 2°$ and 4°), yet stays remarkably coherent and laminar well into the wake due to the low Reynolds number. (The slight pooling seen ahead of the sting at $\alpha = 4°$ is believed to be due to the upstream effects of the larger diameter engine housing at this location.) Clearly, no leading edge vortex could be seen for this angle-of-attack. At higher angles, the apex flow downstream of the canopy turns towards the fuselage surface (side views, for $\alpha = 6°$ and 8°), indicating continued attached flow and suction development. It is also of interest to note here that for $\alpha = 4°$, the red-dye flow in the wake continues to proceed spanwise past the trailing edge crank. The yellow dye approximately represents the blended wind-body junction flow in which we cannot see a corner

https://doi.org/10.1017/S0001924000008095 Published online by Cambridge University Press

vortex at this low angle-of-attack. As the angle-of-attack is increased to $\alpha = 6°$, the flow symmetry is largely retained, but more dye spreading occurs in the wake. In Fig. 2 for $\alpha = 6°$, the red and blue dyes appear on the trailing edge sections of both wing-tips pointing to the possibility of tip-stall on both wings. Since tip-stall has been noted by others at very low angles of attack (Ol[5], Wong, *et al*[9], it was explored further to identify the mechanisms involved.

Figure 3 is an enlarged view of the flow in the near-wake of the wing at $\alpha = 6°$. In following the red dye on both sides, one can see that there is a highly vortical layer that emanates from near the discontinuity at the trailing edge crank in its boundary-layer portion, even as the outer potential flow lines (inboard red lines in this case) move into the wake with little spreading. Its trace is also visible in the side view image (see Fig. 2) for this case. Slightly downstream of the crank, the vortical flow abruptly bursts (at the white arrowheads shown) – inside the triangular region bounded by the crank, wing tip and aft fuselage section. It is evidenced by the wide conical spreading of the red-dye. The expanding flow engulfs the neighboring fluid also, as it rushes towards the wing tip. Consequently, the other dyes are also present there. This is the first clear documentation of tip-stall onset process on this geometry at $\alpha \approx 6°$. By $\alpha = 8°$, in Fig. 2, the extent of tip stall expands upstream nearly parallel to the leading edge. The black dye from the underside is also now intertwined in it through wake flow interactions and is moving upstream along the wing. There is still no evidence of a conical leading edge vortex as is normally reported by this angle-of-attack.

Another steady flow experiment at Re = 13,000 wherein the black dye was introduced at the starboard wing tip confirmed the above observations as the UCAV 1303 angle-of-attack was increased statically as shown in Fig. 4. Initially it moves downstream (see $\alpha = 4°$ case). As the angle is increased, it shows that the black dye at the wing tip starts spreading and moves upstream (see $\alpha = 6°$ case) only after the red-dye reaches the wing tips trailing edge inducing tip-stall. The upstream flow for this situation was found to be sufficiently rapid confirming that tip stall was quite strong, $\alpha = 10°$. At all four Reynolds numbers tested, tip stall was found to occur in a similar way. The interesting aspect of the high Reynolds number flow cases was that there was also a fairly strong flow towards the engine/fuselage at low angles ($\alpha \approx 2°$) and then, the flow reversed dramatically causing tip-stall. Even though flow visualisation is qualitative, the pictures in hand convincingly demonstrate the above described peculiar trend of the trailing edge region flow changing directions near the crank and moving away from the fuselage towards the wing tips for all higher Reynolds number cases investigated. There is a slight dependence on the angle-of-attack for these events.

Analysis of a dye flow movie past a very slowly pitching model ($\alpha + < 0{\cdot}002$; i.e. quasi-steady flow) at Re = 13,000 also supported the above flow description both in regards to tip-stall and before it. As before, the red dye first starts moving angularly towards the trailing edge crank at $\alpha \approx 4°$.

Analysis of the dye flow pattern for $\alpha = 6°$ at Re = 4,100 showed an extraordinarily interesting result; that it compares almost perfectly with the computed surface shear flow pattern presented by Petterson[8] for a Mach number of 0·25, $\alpha = 10°$ and at a vastly higher Reynolds number of 16 million, Fig. 5. As stated earlier and indicated by others[4,5], the dye does not migrate much above the surface indicating a strong viscous/inviscid interaction. It is reiterated that some of the dye flow pattern indicates the surface flow details here.

3.2 Leading-edge vortex

As the angle-of-attack is increased further, a leading vortex forms between $\alpha = 10°$ and $\alpha = 12°$ for Re = 4,100 case. The formation angle-of-attack actually depends on the Reynolds number, moving to slightly lower angles as Re increases. In the data presented in Fig. 2 for $\alpha = 10°$, one can see that the details of the vortex formation are not as is classically described. Here, it appears that

https://doi.org/10.1017/S0001924000008095 Published online by Cambridge University Press

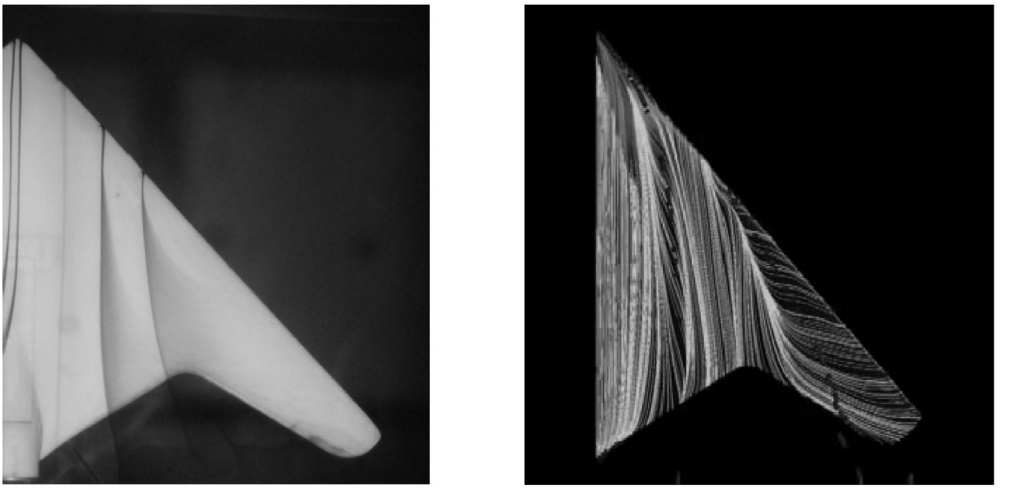


Figure 5. Experiments, U_∞ = 2in/s, α = 6°, Re = 4·1 × 10^4; Right: M = 0·25, α = 10°, Re = 1·6 × 10^7.
(AIAA-2006-1259, Petterson)

just a portion of the leading edge boundary layer significantly downstream of the apex near the wing tips rolls up and not the entire shear layer from the apex region as seen for slender delta wings. The red-dye streaks indicate that the vortex has wrapped and reattached closer to the fuselage in the aft portion of the wing, while the green and blue dyes continue to behave like they did upstream on the wing, at lower angles near; however, they become part of the vortex further downstream (see also side view images for these and other angles in Fig. 2). A spiral structure is visible near trailing edge, but it is unclear if it has burst over the wing. The black dye has moved back into the wake at this lowest Re tested. The vortex wrapping (roll-up) location moves upstream with increase in angle-of-attack (see α = 12° and 15° cases). Near α = 15°, the side view image shows that the black dye splits between the lower and upper surfaces and only beyond this angle-of-attack, it wraps completely around the leading edge as can be inferred by the blue dye pattern. As the vortex grows in size, especially near the trailing edge, the apex flow is also drawn into it near the engine inlet and the upper surface becomes dominated by this vortical flow. The above described flow structural changes result in increasing normal force as will be discussed later. A spiral vortex breakdown appears which moves upstream as expected with increase in angles of attack for beyond this point. Even at 30° angle-of-attack, the apex flow is partially attached over the canopy, but it eventually separates (see α = 35°). These details compare well with those provided by OI[5] although the Reynolds number in Ref. 5 was up to 32,000. OI[5] also concluded that the vortex was weak, but when videos of the flow over our quasi-steadily pitching model were reviewed, a strong reverse axial flow was noticed and hence, it is deemed to be stronger in our experiment. It is not known if the observed differences are due to a smoother model surface finish. As stated before, a very thin polyurethane coating was applied to the model to smooth the surface roughness generally created by the rapid prototyping fabrication process. It may also have rounded the leading edge (measured to be 1/64in as stated earlier) relative to the model in Ref. 5. Past the vortex formation event, the details of the flow behaviour seem as described by Gursul *et al*[2], Taylor *et al*[4] with regard to reattachment moving towards the model centerline and possible secondary and tertiary separation. However, the vortex bursts at a much higher angle than indicated by those authors even for this low Reynolds number of 4,100. These trends were seen at higher Reynolds numbers also suggesting that the UCAV1303 flow wing vortex structure does not behave as seen for a slender delta wing.

https://doi.org/10.1017/S0001924000008095 Published online by Cambridge University Press

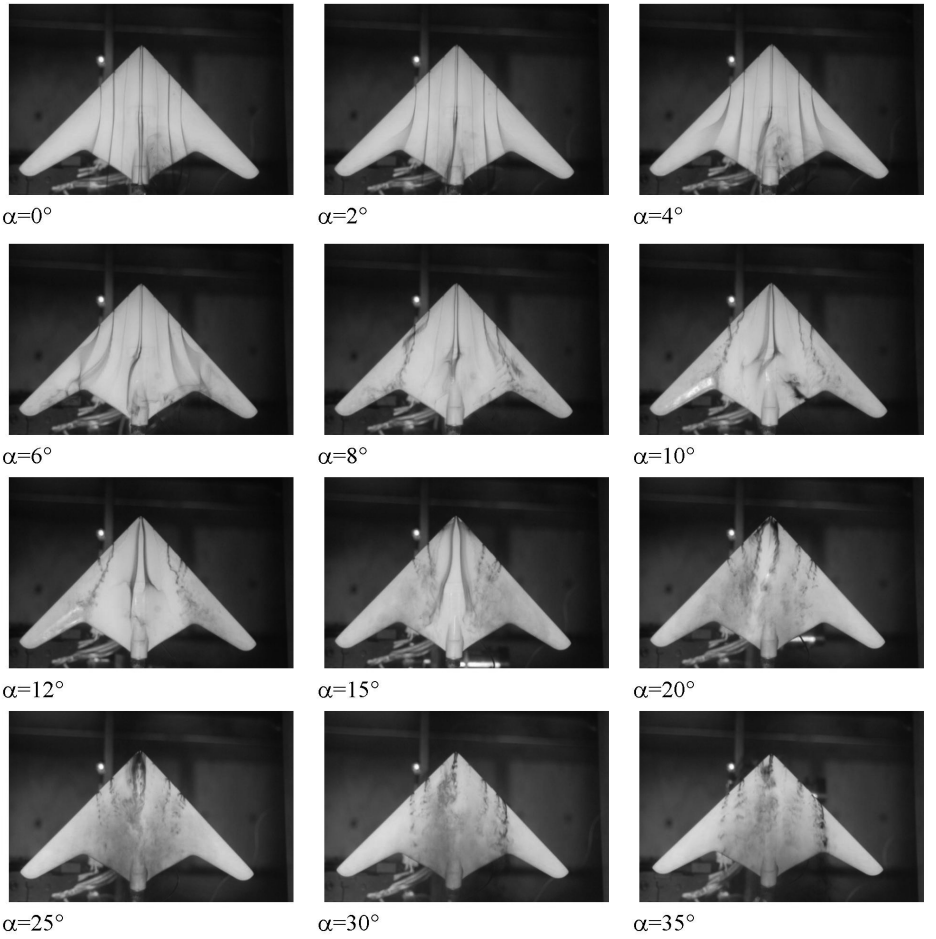


Figure 6. Flow over UCAV 1303, U_∞ = 6in/s, Re = $1{\cdot}3 \times 10^4$.

A full sequence of the flow is presented in Fig. 6 for a higher freestream flow condition, U_∞ = 6in/sec and Re = 13,000. By α = 2°, it is possible to see some spanwise flow at the trailing edge from the back of the fuselage. At α = 4°, the presence of the red-dye at the starboard wing tip points to the onset of mild tip-stall. The flow is still well behaved towards the front of the wing. By α = 6°, tip-stall is clear and the outboard wing dye pattern appears like the footprint of the vortex, which is seen more clearly at α = 8°. As stated earlier and indicated by others[4,5], the dye does not migrate much above the surface indicating a strong viscous/inviscid interaction.

In further analysing the flow visualisation images, it becomes apparent that there is a strong reversed flow present (see black dye in case of α = 10° in Fig. 6) inboard of the crank towards the fuselage. Like before, the black dye was introduced from the lower surface – at a location corresponding to the red dye on the upper surface. Side views show it to be flowing generally into the wake at low angles. It also turns back and flows on to the upper surface as confirmed by the top view presented here at α = 10°. The sequence indicates possible vortex formation beyond α = 8° as both plan views and side views show different dyes wrapping around each other. At a slightly higher angle, the black dye gets folded into the roll up process. Flow pattern behaviour at higher angles was found to be similar to that at lower Reynolds number.

https://doi.org/10.1017/S0001924000008095 Published online by Cambridge University Press

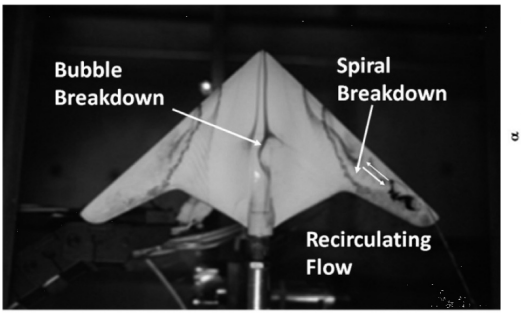


Figure 7. Bubble and spiral type breakdown; $\alpha = 12°$, $U_\infty = 6$in/s, Re $= 1{\cdot}3 \times 10^4$.

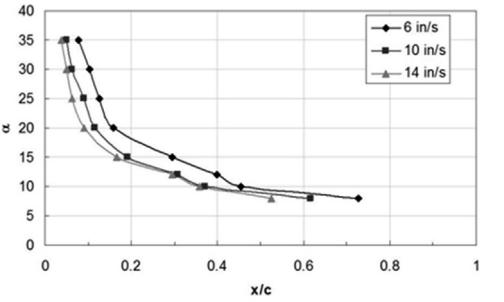


Figure 8. Vortex bursting location *vs* Reynolds number.

3.3 Vortex breakdown

It appears that for this higher Reynolds number (13,000) case, the apex flow (blue dye), follows the canopy and stays attached to the fuselage for a greater distance than for Re = 4,100. A small amount of flow separation for up to $\alpha = 4°$ develops over the fuselage past the canopy as the flow passes into the wake. At slightly higher angles-of-attack, an elongated, skewed bubble forms when it reattaches downstream ahead of the engine. The bubble eventually breaks at $\alpha \approx 8°$ in what appears to be an event independent of the leading-edge vortex (see Fig. 5). At low angles of attack, bubble bursting is the only flow breakdown observed and it is confined to the region around the fuselage. The enlarged view of Fig. 7 (drawn for α around 12°) indicates its presence even at higher angles, after the leading-edge vortex has formed and begun to breakdown as a spiral. Figure 6 shows some changes beyond this angle for the apex flow.

Analysis of video images of the flow as the aerofoil angle-of-attack is increased also revealed the details shown in Fig. 7. There is a fast moving reversed flow from the wing tip towards the apex (black dye) near the leading edge region possibly originating from the tip-stall discussed earlier, whereas over the middle of the wing, the flow passes normally in the streamwise direction. Further back, the dye spreads laterally towards the wing/fuselage junction as already discussed earlier. The leading-edge vortex burst is also simultaneously present. It is interesting to observe both known bursting mechanisms co-exist on the same wing side at some of the angle-of-attack studied. The dramatic spanwise movement of the flow until large angles (for all cases studied, see Fig. 2 and Fig, 6 for example) over the wing towards and away from the fuselage is very intriguing. It is also difficult to find a specific pattern to these flow direction swings. Even though the vortex breakdown pattern followed the general trend seen over slender delta wings, it was considerably more difficult to generate plots of vortex bursting locations vs angles of attack.

The vortex bursting location (although quite difficult to precisely determine) exhibited dependence similar to what was observed in case of slender delta wings on Reynolds number as shown in Fig. 8. However, this dependence was much weaker here.

3.4 Effect of steady roll

In an effort to assess the flow behaviour, the model was taken through both steady and dynamic roll motions. Typically roll towards the starboard side was used because the side-view camera then provided a clear view of the upper surface flow details. In steady flow, the roll angle was set to 10°, 20° or 30° and the model angle-of-attack was varied from 0 – 35°, capturing both upper-side and side-view images at selected angles-of-attack. Dynamic roll at non-zero angles of attack also

https://doi.org/10.1017/S0001924000008095 Published online by Cambridge University Press

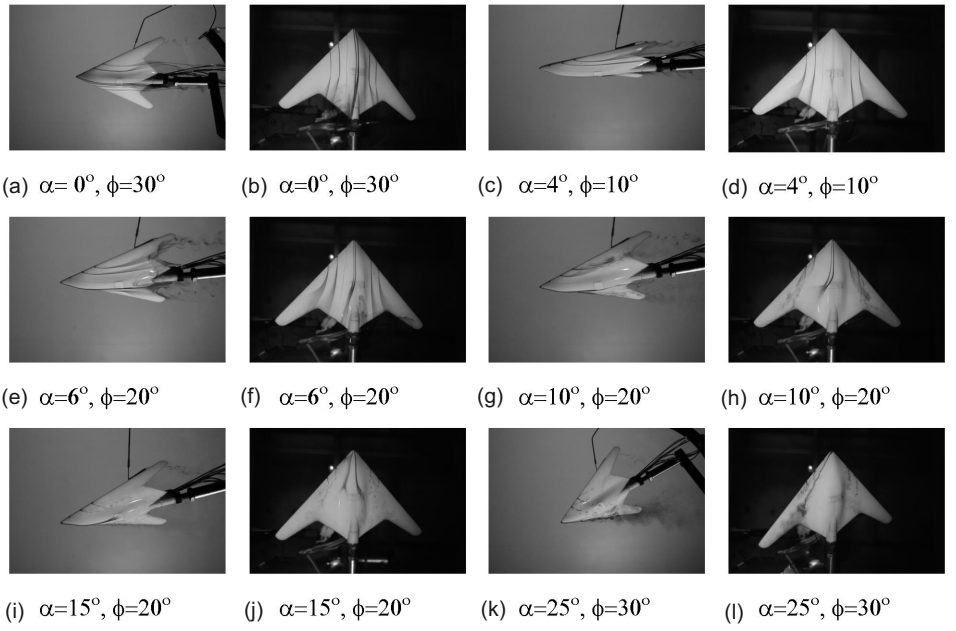


Figure 9. Effect of roll angle on flow; U_∞ = 6in/s, Re = $1{\cdot}3 \times 10^4$.

resulted in a coning motion, due to the design of the drive. Here, only steady flow results will be discussed for selected cases.

Due to the roll angle used, the flow starts migrating towards the port side in general, an effect seen at low angles as observed in Fig. 9(a) and 9(b). As angle-of-attack is increased to 4° (Fig. 9(c) and 9(d)), signs of tip-stall (see red-dye) are observed for the low roll angle case, which moves to 6° for the 20° and 30° roll angle cases. Interestingly, Fig. 9(c), 9(e) and 9(f) depict its onset from breakdown of the shear layer over the starboard side. The details of this were discussed earlier. However, no tip stall is seen on the port side. Implying that the flow that migrated towards the port side tip has now moved away from it at angles of attack. But, the large spanwise flow akin to that seen for the no roll case is present. Thus, one can expect measurable side forces due to this flow difference at these angles. Figure 9(e) suggests that the outboard port side flow is beginning to break down just as it enters the wake. The apex flow seems quite lopsided as it moves to the port side. By 10° (Figs 9(g) and 9(h)), the vortical flow has already broken down for the 20° roll case. Interestingly, for all cases, at 15° angle-of-attack, the split apex flow as seen in Fig. 9(i) and 9(j) were seen, the cause of which is not clear. At $\alpha = 25°$, $\phi = 30°$, it is easy to see that the apex flow has once again reverted toward the port side, its vortical breakdown is similar to what is normally seen as spiral type over slender delta wings (unlike the bubble type discussed earlier). These general flow attributes were common to all cases studied.

3.5 Effects of steady yaw

Yaw manoeuvre studies at a fixed pitch angle of 0° indicated the presence of strong side-slip that was observed for steady flow cases. It also appeared that the effects were stronger at the higher Reynolds numbers with the apex flow showing the most deviation from the straight path towards the yaw direction used. No other effects could be seen. These may appear as the angle-of-attack and roll angle are increased.

https://doi.org/10.1017/S0001924000008095 Published online by Cambridge University Press

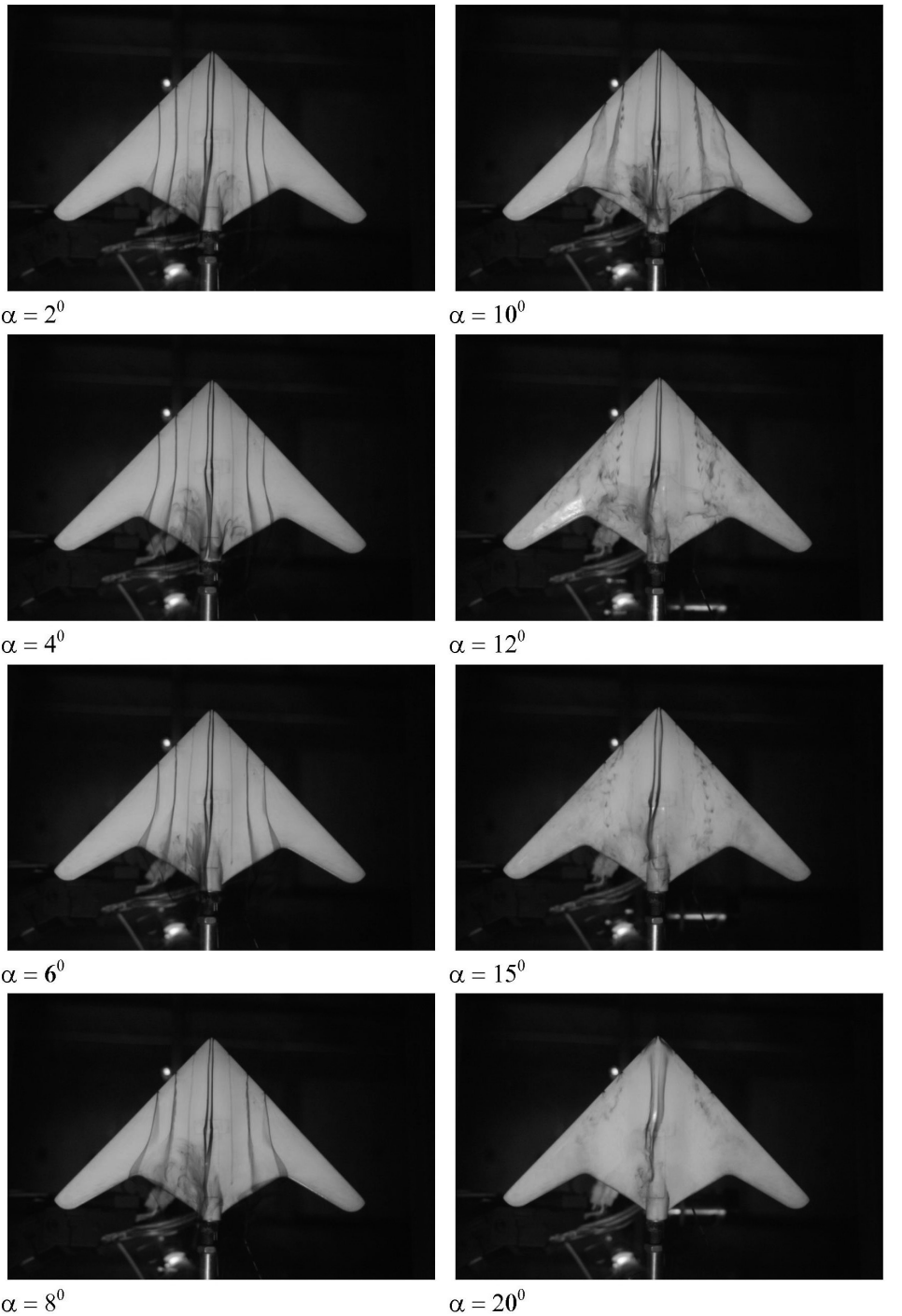


Figure 10. Flow evolution over a dynamically pitching UCAV 1303 model; U_∞ = 6in/s, α^+ = 0·05 Re = 1·3 × 10^4.

https://doi.org/10.1017/S0001924000008095 Published online by Cambridge University Press

3.6 Dynamic manoeuvre studies

Flow visualisation studies were conducted for pitch-up manoeuvres. The pitch rate (and likewise the roll rate) used here was defined here as:

$$\alpha^{+} = \dot{\alpha}c/U_{\infty}$$

Typical rates used were 0·05 and 0·1. The pitch angle of the manoeuvring UCAV was varied in a ramp type manoeuvre to investigate dynamic pitch rate effects on the UCAV flow field. For this investigation, the model was pitched from $\alpha = 0°$ to $\alpha = 30°$, while photographs were taken at the angles under investigation. The model was then pitched from $\alpha = 30°$ to $\alpha = 0°$, while photographs were again taken.

Figure 10 shows flow visualisation pictures for the case of at a non-dimensional pitch rate $\alpha + = 0{\cdot}05$ for U_{∞} = 6in/s, Re = $1{\cdot}3 \times 10^4$ to enable a one to one comparison with steady flow at the same freestream flow conditions. Some very intriguing flow aspects appear in the pitching cases. Firstly, the spanwise flow that appeared at angles-of-attack as low as 2° and eventually led to tip stall is not present. Only a slight tendency of this can be seen towards, but further downstream of the trailing-edge crank. The fuselage flow seems more vortical in the wake, and its upstream effects appear locally near the engine exit. The picture remains nearly identical until $\alpha = 8°$ (for this pitch rate) when inboard spanwise flow becomes clear along the trailing edge and in the wake. An almost dramatic right angled inward flow turn develops for $\alpha = 10°$ (see red dye), but it remains clearly away from the wing tip. This flow actually turns upstream for some other flow conditions. Side views (see Fig. 11 below) for $\alpha = 8°$ and $\alpha = 10°$ show that the spanwise directed flow is originating from a vortex.

This extremely preferential flow direction was observed for all cases studied and cannot be explained easily since a bursting vortical flow must spread in all directions. It then implies the

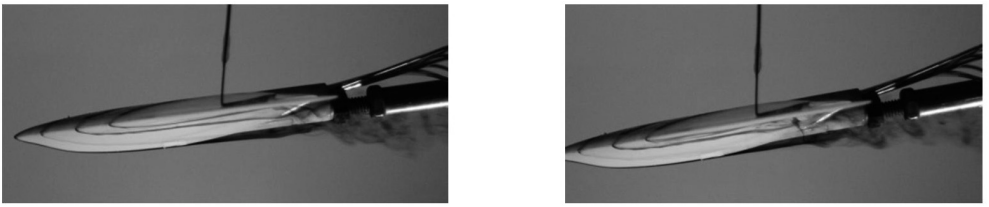


Figure 11. Pitching 1303 model flow side views; U_{∞} = 6in/s, α^{+} = 0·05 Re = $1{\cdot}3 \times 10^4$.

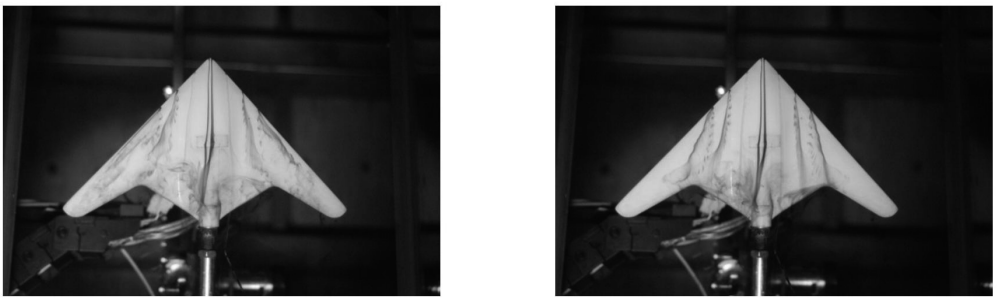


Figure 12. Combined pitch-roll manoeuvre, U_{∞} = 6in/s, Re = $1{\cdot}3 \times 10^4$, $\alpha = 10°$, $\phi = 10°$; Roll to starboard side.

https://doi.org/10.1017/S0001924000008095 Published online by Cambridge University Press

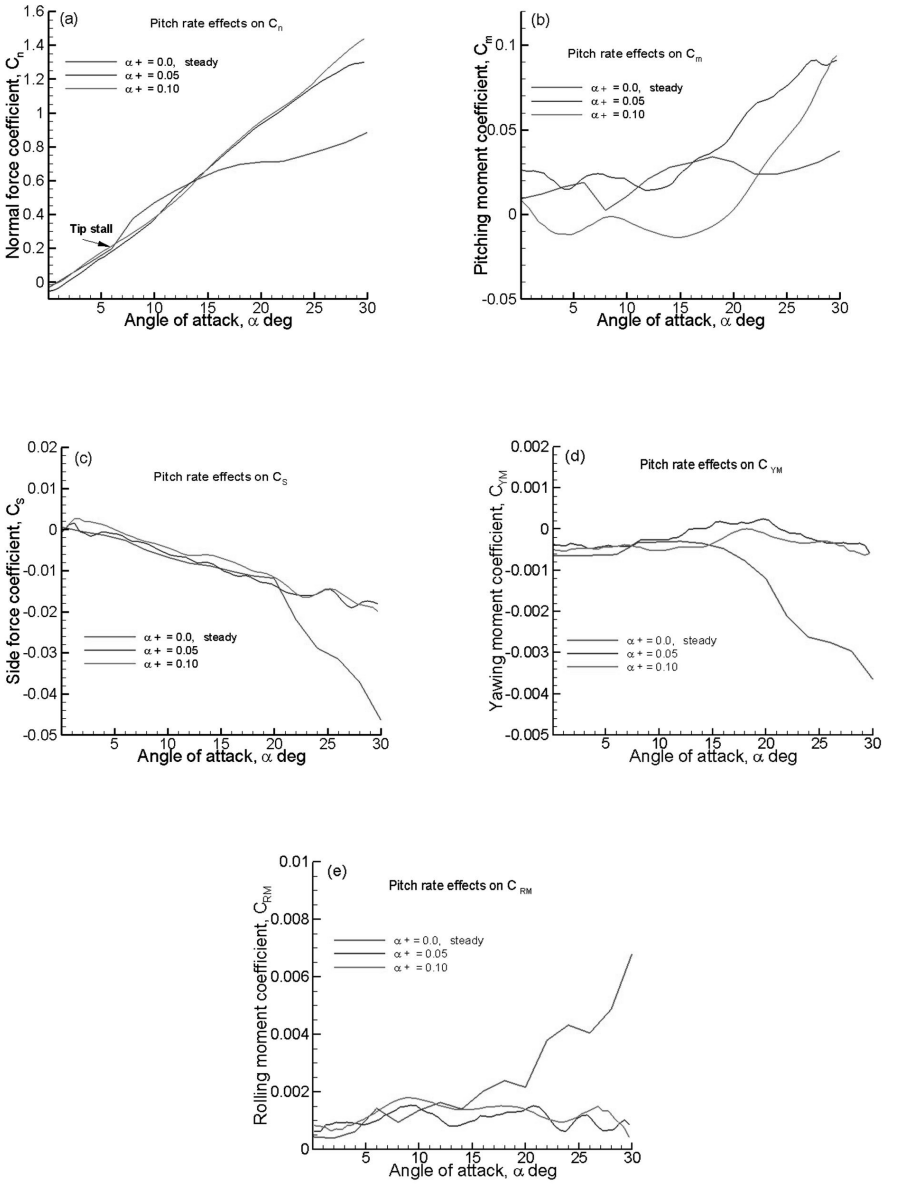


Figure 13. Various aerodynamic coefficients vs angle-of-attack over steady and ramp-type pitching UCAV 1303 model, U_∞ = 10in/s, Re = $2{\cdot}3 \times 10^4$, $\alpha^+ = 0{\cdot}05$ (blue), $0{\cdot}01$ (green).

presence of a strong pressure gradient that drives the flow towards the fuselage and away from the tip. However, at the slightly higher angle-of-attack of $\alpha = 12°$, the characteristic leading edge vortex that was described earlier for the steady flow appears around this angle and then, the flow first breaks down near the tip region at higher angles as can be inferred from the spreading of the red dye there. Also, in contrast to the steady flow details for the same model, a movement towards and away from the fuselage was not observed. For most part, the flow remains parallel and as the vortex grows, the green and blue dye streams are entrained into it. At high angles of attack ($\alpha = 20°$), the apex

https://doi.org/10.1017/S0001924000008095 Published online by Cambridge University Press

flow experiences a spiral vortical breakdown unlike in steady flow where it was bubble type as indicated for steady flow in Fig. 7. The absence of tip stall was seen for all pitch rates studied and all freestream flow conditions tested. The occurrence of such a flow pattern slightly changed with speed (to lower angels) and non-dimensional pitch rate (higher angles). This absence of tip stall must translate into a different load behaviour, which will be briefly discussed later.

In addition, roll and yaw manoeuvres were carried out at roll rates of 3deg/s, 5deg/s and 7deg/sec. Various combinations were tried and only some specific cases are discussed below.

The model was set to steady roll angles and pitched from 0 to 30° at rates of 3deg/s and 7deg/s. The yaw angle was maintained at zero deg. The results are shown in Fig. 12. During this combined manoeuvre investigation, Fig. 12 shows that at an angle-of-attack of 10° and a roll angle of 10°, LEV formation is observable. The higher pitch rate, as with the pitch only manoeuvre case investigated, has significantly delayed vortex formation and bursting, lowered the amount of flow separation along the outer winzg regions and reduced wing tip stall. The wing flow typically moves towards the upper wing tip as seen here also which is likely to induce tip-stall on the port side for this case. However, the starboard tip stall is relieved and it is clearly seen that the flow is moving towards the fuselage from the crank instead of towards the tip.

3.6 Aerodynamic load studies

As described earlier, using a five-component balance, load data was collected in steady flow at different velocities, dynamic pitch as well as roll manoeuvres, but in this section, only results for steady flow at U_∞ = 10in/sec (Re = 2·3 × 10^4) and selected pitch-up manoeuvres at this velocity will be discussed. For dynamic pitch-up studies, experiments helped establish that 20 cycles were adequate for ensemble averaged data to become statistically stationary; thus all unsteady load data reported have been averaged over 20 cycles for the results reported.

Normal force coefficients are presented in Fig. 13(a). As can be seen in it, the 1/72nd scale model UCAV 1303 produces C_n values comparable to that measured at larger scales and at higher Mach number and Reynolds numbers (see Refs 7, 8). A clear normal force break is seen at around $\alpha = 6°$, attributable to tip-stall. In Sec. 2·A, the slight dependence of tip-stall on Reynolds number was referred to. It is evident in the load measurements as well at 6° for this higher velocity case, instead of 4° for the lower Re case discussed in the flow visualisation pictures. Once the flow recovers, the next change of slope seems associated with vortex formation. C_n continues to increase with α but at a slower rate than before probably due to the weak leading edge vortex that was discussed earlier. The behaviour appears to be remarkably non-linear. On the contrary, when the model is dynamically pitched from 0 to 30°. angle-of-attack, C_n exhibits a surprisingly linear variation, but in two sections. Around $\alpha \approx 12°$, when the vortex forms, a slope change occurs. In comparing the flow features and the normal force curves, it seems that the apex vortex is stronger in case of the ramp-type pitch up cases and this leads to a higher normal force. However, no tip-stall related changes can be seen, confirming the flow visualisation result that it is not present or is insignificant. Also, for both $\alpha+ \approx 0{\cdot}05$ and $\alpha+ \approx 0{\cdot}1$, the C_n behaviour is nearly identical. Only at large angles, when vortex bursting details are likely to be different do changes appear.

Correspondingly, the pitching moment coefficient C_m (Fig. 13(b)) behaviour also supports the above inferences. The appearance of tip-stall in steady flow induces a well defined pitch-break, but C_m recovers as the angle-of-attack increases. For the steady flow case, the variation of C_m is qualitatively similar to that reported by Pettersen[8]. The negative $\partial C_m/\partial\alpha$ seen for the steady case at $\alpha \approx 18°$ seems to be absent when the model is pitched, with the value remaining positive throughout and also, rising steeply with angle-of-attack, due to the low pressure near the apex attrib-

https://doi.org/10.1017/S0001924000008095 Published online by Cambridge University Press

utable to the vortex. This confirms the distinctly different vortex behaviour when the model is dynamically pitched. The side force C_S, the yawing moment coefficient and C_{YM} the rolling moment coefficient C_{RM} (Figs 13 (c), (d) and (e) all show much softer variations in dynamic cases compared to the steady case at higher angles of attack. The continued low value of the rolling moment beyond $\alpha = 15°$ suggests that the vortex flow is symmetric. The side-slip is also smaller and even the yawing moment is small for the dynamic cases. However, pitching moment behaviour points to an increased unstable tendency overall.

4.0 CONCLUSION

- Flow visualisation and load measurements over a UCAV 1303 model in a water tunnel were obtained for a range of experimental conditions.
- Flow features which are different from the ones reported in the literature were observed, especially in regards to the formation and bursting of the vortex.
- The model stalled first with tip-stall occurring at a very low angle-of-attack. Onset of tip-stall has been shown to arise from spanwise outboard flow towards the wing tips induced from the shear-layer vortex breaking slightly aft of the trailing edge crank. This also manifests in a normal force break at the corresponding angle-of-attack. The process has a slight dependence on the Reynolds number.
- The leading-edge vortex behaviour is unlike that seen for slender delta wings. It forms a notable distance from the wing apex and moves upstream, while lying close to the surface due to viscous/inviscid interactions. The vortex appeared to be tightly wound and small, stayed close to the upper surface, with strong axial reversed flow present. But, it burst quickly at low angles of attack (10-12°) unlike a slender delta wing. The bursting process lingers over the wing through a modest increase in angle-of-attack.
- The flow exhibits movement towards and away from the fuselage in a manner difficult to predict. Prior to vortex bursting, it was moving away from the fuselage. But, when it vortex began to burst, the flow curved towards the fuselage. This rapid movement of the flow may be expected to cause unexpected fluctuations in loads and moments.
- Pitching the model at different rates yielded results similar to the slender wing cases by delaying vortex breakdown. Most importantly, the tip stall appeared to be eliminated.
- The dynamic side force, rolling moment and yawing moment coefficients were all more favorable compared to the static case. However, a strong rise in the pitching moment was observed for the dynamic cases indicating an increased tendency towards instability.
- Rolling to one side seemed to help alleviate tip stall on the wing tip that went down.
- Increasing Reynolds number moved vortex bursting at a given angle towards the trailing edge.

ACKNOWLEDGEMENTS

Funding for the project (TDSI/07-005/1A) was provided by the Singapore TDSI/Temasek Group under a CRADA with the US Naval Postgraduate School. This is gratefully acknowledged. The authors express their thanks to the USAF for supplying the model geometry file. The authors also thank LT. Phil Sosebee, US Navy & NPS for successfully duplicating and confirming some of the earlier results.

https://doi.org/10.1017/S0001924000008095 Published online by Cambridge University Press

REFERENCES

1. CUMMINGS, R.M., MORTON, S.A and SIEGEL, S.G. Numerical prediction and wind tunnel experiment for a pitching unmanned combat air vehicle, *Aerospace Science and Technology J*, December 2008, **12**, pp 355-364.
2. GURSUL, I., GORDNIER, R. and VISBAL, M. Unsteady aerodynamics of non slender delta wings, *Progress in Aerospace Sciences*, 2005, **41**, pp 515-557.
3. YANIKTEPE, B. and ROCKWELL, D. Flow structure on a delta wing of low sweep angle, *AIAA J*, March 2004, **3**, pp 513-523.
4. TAYLOR, G.S. SCHNORBUS, T. and GURSUL, I. An investigation of vortex flows over low sweep delta wings, AIAA 2003-4021, June 2003.
5. OL, M.V. Water Tunnel Velocimetry Results for the 1303 UCAV Configuration, AIAA-2006-2990, June 2006.
6. GHEE, T.A. and HALL, D.R. Experimental and numerical investigation of vortex shedding of a representative UCAV configuration for vortex flow control, Proc. RTO AVT Symposium on Advanced Flow Management: Part A- Vortex Flows and High Angle-of-Attack Military Vehicles, Loer, Norway, RTO-MP-069(I), May 2001.
7. MCPARLIN, S.C., BRUCE, R.J., HEPWORTH, A.G. and RAE, A.J. Low speed wind tunnel tests on the 1303 UCAV concept, AIAA 2006-2985, June 2006.
8. PETTERSON, K. CFD analysis of the low-speed aerodynamic characteristics of a UCAV, AIAA 2006-1259, January 2006.
9. WONG, D.W., MCKENZIE, G.J., OL, M.V., PETTERSON, K. and ZHANG, S. Joint TTCP CFD Studies into the 1303 UCAV Performance, AIAA 2006-2984, 2006.
10. CUNNINGHAM, Jr., A.M. and BUSHLOW, T. AIAA-90-2815-CP, 1990.
11. MCLAIN, B.K. Steady and Unsteady Aerodynamic Flow Studies over a 1303 UCAV Configuration, MS Thesis, US Naval Postgraduate School, September 2009.
12. CHUA, W.H. Flow visualization studies over a UCAV 1303 model, M.S. Thesis, Naval Postgraduate School, 2009.
13. CARR, L.W. and CHANDRASEKHARA, M.S. Compressibility effects on dynamic stall, *Progress in Aerospace Sciences*, 1996, **32**, pp 523-576.
14. KRAMER, B. and KERHO, M. Five-component balance system for water tunnel Applications: General Instructions and User's Manual Rolling Hills Research Corporation, February 2001.

https://doi.org/10.1017/S0001924000008095 Published online by Cambridge University Press